Applied Physics A (2018) 124:426
https://doi.org/10.1007/s00339-018-1840-x

Applied Physics A
Materials Science & Processing

Fabrication of locally micro-structured fiber Bragg gratings by fs-laser machining

Franz J. Dutz[1] · Valentin Stephan[2] · Gabriele Marchi[1] · Alexander W. Koch[3] · Johannes Roths[1] · Heinz P. Huber[2]

Received: 30 January 2018 / Accepted: 7 May 2018 / Published online: 15 May 2018

Abstract
Here, we describe a method for producing locally micro-structured fiber Bragg gratings (LMFGB) by fs-laser machining. This technique enables the precise and reproducible ablation of cladding material to create circumferential grooves inside the claddings of optical fibers. From initial ablation experiments we acquired optimized process parameters. The fabricated grooves were located in the middle of uniform type I fiber Bragg gratings. LMFBGs with four different groove widths of 48, 85, 135 and 205 µm were produced. The grooves exhibited constant depths of about 30 µm and steep sidewall angles. With the combination of micro-structures and fiber Bragg gratings, fiber optic sensor elements with enhanced functionalities can be achieved.

1 Introduction

Fiber-optic sensors (FOS) promise high potential for operating in industrial fields of application such as the energy sector [1, 2], structure monitoring [3, 4], medicine and biology [5–7]. Typical benefits of FOS lie in their multiplexing capability, their miniaturized sensor design and their resistance to electromagnetic interference. Among FOS, fiber Bragg grating (FBG) sensors are mainly applied for sensing temperature and mechanical strain by detecting the shifts of the Bragg wavelengths [8].

According to Young's law, there is a linear relationship between stress and strain of a spring element. Considering the fiber as spring element, FBGs can operate as force sensors. For a given axial force, the axial strain of the fiber depends on the cross section of the fiber; the smaller the cross section, the higher the strain. With standard FBGs, temperature and force effects are difficult to separate because the Bragg wavelength depends on both strain and temperature. Several approaches to discriminate strain (force) and temperature using FBG-based sensors have been reviewed by Frazao et al. [9].

An improvement of the sensing functionality of uniform FBGs has been demonstrated with so-called locally micro-structured FBGs (LMFBGs) [10]. At the location of the FBG, LMFBGs comprise a small fiber segment with a reduced diameter that is shorter than the extension of the FBG in order to generate a specific change of the grating period when axial forces are applied. These structures have been produced by different techniques, including chemical etching [11] and tapering [12]. Employing laser-structuring of the polyamide coating of the fiber and using it as a mask for a HF-based etching process, Iadicicco et al. [13] have fabricated a 136 µm long microstructure with 6 mm in diameter within a 6 µm long FBG inscribed in a standard fiber of 125 µm in diameter. Cusano et al. [12] locally tapered a standard fiber by electric arc discharge (EAD) and achieved over lengths of typically 350 µm reduced fiber diameters down to 50 µm. These microstructures divide the pristine FBG into two sub-FBGs that form a Fabry–Perot structure and the local microstructures introduce phase shifts between the waves reflected from both mirrors of the Fabry–Perot. The reflection spectrum of the LMFBG shows a pass band within the stop band of the pristine FBG for non-zero phase shifts. The spectral position of the pass band depends on the phase difference between the waves from both sub-FBGs and the strength of

✉ Franz J. Dutz
franz_josef.dutz@hm.edu

Heinz P. Huber
heinz.huber@hm.edu

[1] Photonics Laboratory, Munich University of Applied Sciences, 80335 Munich, Germany

[2] Lasercenter, Munich University of Applied Sciences, 80335 Munich, Germany

[3] Institute for Measurement Systems and Sensor Technology, Technical University of Munich, 80335 Munich, Germany

the pass band depends on the balance of the intensities of both reflected waves. Sensing of the surrounding refractive index [14] and temperature self-referenced strain measurements have been demonstrated [12] by using LMFBGs. Although a qualitative agreement between measured reflection line shapes and theoretical considerations has been shown [11], theoretical model calculations that fit to the measured line shapes have not yet been reported. Both fabrication methods mentioned above produce gradual transitions between the pristine fiber and the fiber segment with the reduced diameter. The lengths of the transition regions are typically larger than the segments with the reduced diameter, hindering to find a quantitative model of the sensor structure and thus a theoretical description of the reflected spectrum. Additionally, the design flexibility of the sensor structures and the reproducibility of the fabrication processes remain limited [15].

Over the years, femtosecond (fs) micromachining has become an important tool in the fabrication of advanced photonic devices in transparent materials [16]. Applications in fiber-optic sensor design have been, e.g. the inscription of fs-FBGs [17, 18], micro Fabry–Perot interferometers [19, 20] and complicated structures with micrometric precision [21, 22]. Some of the authors have already proposed and demonstrated a LMFBG manufactured by femtosecond laser micro-structuring [23]. The sensor structure has been designed for the measurement of compressive forces for biomedical applications [7]. The short pulse duration avoided excessive heating of the material and consequently preserved the FBG within the structure from damage. The precise shapes of the structures and the sharp boundaries between the fiber segments enabled the development of a transfer matrix model comprising of three sections, the left and right sub-FBGs and the structured section in the middle. This theoretical model allowed a very good description of the spectral response of the LMFBG with temperature and force as the free fit parameters. It was possible to achieve a separation of force and temperature measurement [23, 24] by applying the model and fitting model-based reflection line shapes to measured data. Because of the reduced diameter in the structured fiber section, this LMFBG also showed an enhanced force sensitivity compared to standard FBG sensors [25].

In this article we describe the systematic and automated method to generate a LMFBG using a fs-laser micro-structuring procedure on standard single mode fibers (Nufern GF1B) containing 1.3–6.8 mm long type I FBGs. Four different LMFBGs were produced by engraving circumferential grooves with lengths of 48, 87, 135 and 205 µm in the middle of the FBGs by fs-laser ablation. The grooves in the cladding of the fiber had constant depths of about 30 µm and steep sidewalls.

2 Experimental setup

The LMFBGs presented in this paper were fabricated in an experimental setup comprising a fs-laser system and a setup for mounting, *xy*-positioning and rotating the fiber. Figure 1 shows a schematic drawing of the system.

The fs-laser source used is a regenerative amplifier (femtoREGEN, High Q Laser, Rankweil, Austria) with an emission wavelength of 1036 nm, a pulse duration of 470 fs and a repetition rate of 60kHz. The laser beam was directed by several mirrors via a beam expander (expansion factor 2.5) towards a microscope objective (MO) with a numerical aperture of 0.6 and a magnification of 32×, which focused the beam on the sample. The beam diameter at the entrance of the MO was about $D_{MO} \approx 10\,\text{mm}$. An integrated dichroic mirror in the collimated beam path, which was reflective for 1036 nm and transparent for visible wavelengths, allowed the observation of the processing site by a CCD camera. The MO was mounted on a vertical stage, and thus the focal point could be shifted in *z*-direction with a precision of about 1 µm.

We placed the setup for the automated rotation of the FBGs on an *xy*-translation stage, which allowed positioning with a precision of about 1 µm in *x*- and *y*-direction. The rotation setup consisted of a step motor rotating the FBG and of two capillary mounts. The capillaries and the axis of the step motor were aligned collinear to each other. The

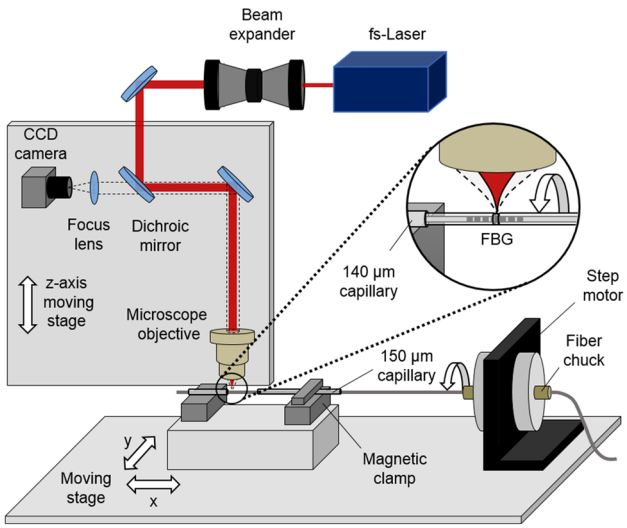

Fig. 1 Schematic drawing of the experimental setup for manufacturing LMFBGs. The experimental setup comprises a step motor driven rotation stage (metal block and angle plate mounted on a work bench, a fiber chuck attached to the step motor), fiber fixture components (capillary with 140 µm inner diameter glued on a metal block, capillary with 150 µm inner diameter held by a magnetic clamp) and the fs-laser source, several beam steering mirrors, a 2.5× beam expander, a CCD camera and a microscope objective (NA 0.6, 32×)

first capillary, which was glued on a block, had an inner diameter of 140 µm. The second capillary, held by a magnetic clamp, had an inner diameter of 150 µm. The FBG was positioned with the help of a check laser (model Fiberpoint 250/HPD, IMM Photonics GmbH, Unterschleissheim, Germany) between both capillaries where the machining of the fiber was carried out.

3 Sample preparation and determination of ablation threshold and spot diameter

Before actually beginning the micro-structuring of FBG sensors, we determined the ablation threshold fluence of a flat fused silica (FS) sample (model WG42012, Thorlabs GmbH, Munich, Germany) with the D^2-method [16]. The evaluation formula of the peak fluence from the measurable laser parameters is given as follows:

$$\Phi = \frac{2 \times \overline{P}}{f_R \times \pi \times w_{eff}^2}, \quad (1)$$

where $\overline{P}$ is the average power measured at the sample; f_R is the repetition rate of the laser system and w_{eff} the effective focus or spot radius. In Fig. 2 the results of threshold fluence measurements are displayed: The linear fit function yields a threshold fluence $\Phi_{thr,FS} = 3.8 \pm 0.3\,J/cm^2$ and an effective focus radius $w_{eff,FS} = 1.45 \pm 0.06\,\mu m$.

The meaning of the effective spot radius is connected with the assumptions of the D^2-method, which are a Gaussian spatial laser beam fluence profile and a pure process threshold behavior: Above a certain threshold fluence the observed process, here the ablation of fused silica, occurs, below the threshold no material is removed. As the laser processing of transparent media bases on multi-photon absorption, a non-linear process, the w_{eff} derived from the fused silica sample might underestimate the beam radius. To access the spot radius of our setup in an independent experiment, we carried out a second D^2 measurement on a well-defined metal sample based on linear absorption (500 nm thick molybdenum film on a glass substrate (MGS) [26]). In the MGS D^2-experiment the effective beam radius was determined to $w_{eff,MGS} = 1.6\,\mu m$, which lies about 10% above the value of the measurement on fused silica and represents the diffraction limit of the focal spot. This value of $w_{eff} = 1.6\,\mu m$ was used to calculate all fluence values mentioned in the following sections.

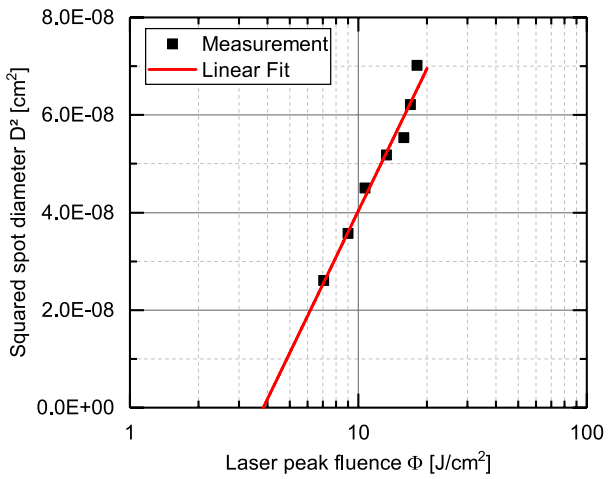

Fig. 2 D^2-method for determining the threshold fluence of a fused silica sample. The linear fit function yields a value of $\Phi_{thr,FS} = 3.8\,J/cm^2$ for the threshold fluence and a value of $w_{eff,FS} = 1.45\,\mu m$ for the effective spot radius

Early studies of the ablation threshold of fused silica for near infrared laser pulses and its dependence on pulse duration in the ultra-short pulse regime have already been performed in the mid-1990s e.g. by Stuart et al. [27]. They have found ablation thresholds for sub-ps pulse durations in the range of 2–3 J/cm^2. More recent works from Varkentina et al. [28] and Mirza et al. [29] have indicated values of 5.9 and 2 J/cm^2 as thresholds for ablation. Our peak fluence value of 3.8 J/cm^2 is in accordance with the reported values.

4 Focus search and machining process

The most critical start coordinate for the fiber machining process is the zero position in z-direction, z_0. Zero position means that the z-position of the optical focus is identical with the highest point of the fibers cross section. It was not possible to identify the focus position with the in-line camera vision system. Therefore, the focus position had to be determined by a so-called focus test routine prior to the LMFBG fabrication. Initially, we placed the fibers surface close but still below to the estimated z-position of the focus. Then, a linear movement in y-direction was performed. This movement has been repeated for several times with subsequently 2 µm lowered z-positions and 10 µm displacement in the y-direction. When the focus had approached the surface of the fiber, the y-scans created a series of grooves on the fibers surface with individual lengths (see Fig. 5a, b, vertical black lines). The vertical position of the MO where the second visible groove was inscribed was chosen as z_0, because it showed the most uniform ablation. The uncertainty of the focus finding routine is estimated to $\pm 2\,\mu m$.

Figure 3 depicts a schematic of the systematic fabrication process of the LMFBGs. The entire process was performed in three steps. At the determined z_0 position, the structuring started by applying the laser pulses on the top of the fiber surface and rotating the fiber. This way, a complete 360° circumferential groove (Fig. 3a) was produced. After ablating the groove, the fiber was shifted by $\Delta x = 2\,\mu m$ for

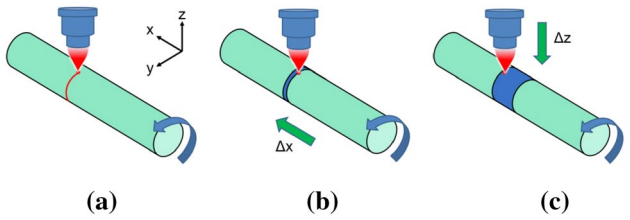

Fig. 3 Schematic of the systematic process for generating the LMFBG: (a) Focusing the laser beam on the fiber surface at z_0 position and performing a complete 360° (ring structuring). (b) Moving the fiber in x-direction by $\Delta x = 2\,\mu$m for the next ring structures intersecting with previous ring structures until a desired groove width was generated. The number of Δx-steps, N_x, defined the groove width. (c) Lowering the MO with $\Delta z = 1\,\mu$m for the next ring structures and repeating the second step until a desired groove depth was reached. The three steps (a)–(c) were repeated N_z times to obtain a desired groove depth

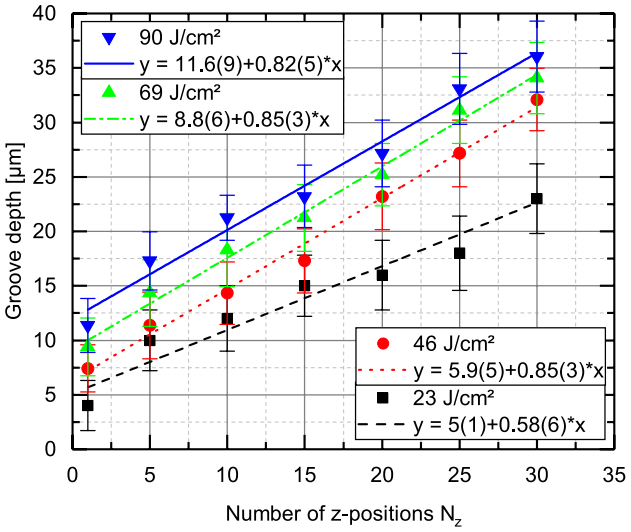

Fig. 4 Process landscape to determine parameters for a desired groove depth. Here, the measured groove depth d is shown in dependence on the number of scans, N_z, for different fluence, Φ. The lines correspond to linear fits to the respective data. In this study, values of $\Phi = 46\,\mathrm{J/cm^2}$ and $N_z = 25$ were selected for a desired groove depth $d = 30\,\mu$m

producing the next groove which intersected with the previous circumferential groove. The process in x-direction was performed until a desired groove width b^* was reached (Fig. 3b). Then, the laser focus position was set at the original xyz-position except that the MO position was lowered by $\Delta z = 1\,\mu$m

(Fig. 3c). At this new position, the processing of circumferential structures at successive positions along the x-axis was carried out again. This whole process has been repeated until a desired groove depth d was achieved. The whole process produced individual grooves with specific groove widths, b, and depths, d. The number of z-positions was identical to the number of scans, N_z, in x-direction and determined the groove depth d, while the number of Δx-steps, N_x, defined the groove width b.

5 Determination of process parameters

For a determination of optimized laser machining parameters such as average power, repetition rate, spot radius and spot scanning speed, expressed as a product of angular velocity and fiber radius, generalized process parameters have to be introduced, which are proportional to the average applied dose in $\mathrm{J/cm^2}$ per position. The generalized laser parameters include pulse overlap OL or, in other terms, pulses per position PPP and the laser fluence Φ. The overlap OL and the pulses per position PPP are related by

$$\mathrm{OL} = 1 - \frac{1}{\mathrm{PPP}} = 1 - \frac{\omega \times r}{f_\mathrm{R} \times 2 \times w_\mathrm{eff}} \tag{2}$$

with f_R as repetition rate, r as the radius of the fiber and w_eff as the effective focus radius determined by the D^2-method to $w_\mathrm{eff} = 1.6\,\mu$m (see Sect. 3). During the entire machining process the fiber rotated with a constant angular velocity of $\omega = 698$ mrad/s (equals $t = 9$s per 360°-turn), which was the fastest value to be set with the rotation stage employed. The resulting OL at the unstructured fiber full radius $r_0 = 62.5\,\mu$m calculates to 99.98%, corresponding to an average pulses per position of PPP=4400 at the beginning. During the processing, the radius decreases to about 32.5 µm and thus PPP increases gradually to 8500. The machining parameters also include the focus shift Δz and the number of Δz-steps, N_z (see Sect. 4). To obtain a process landscape, grooves in standard fibers were manufactured at varying fluencies and numbers of N_z, while the focus shift Δz was set to a constant value of 1 µm.

Figure 4 displays the process landscape consisting of the measured depths of the grooves as a function of N_z for several fluencies, Φ. From the chart in Fig. 4 both parameters, Φ and N_z, can be selected to reach a desired groove depth. As indicated by the linear fit curves, a typical ablation depth of about 0.9 µm per scan could be realized at fluence higher than approximately 50 $\mathrm{J/cm^2}$. By extrapolating the fit curves, an estimate to obtain deeper depths is possible.

In this work the aim was to generate grooves with depths d of 25 µm to 30 µm (leaving a remaining fiber radius of approximately 32.5 µm). Thus, according to Fig. 4, we selected the values $\Phi = 46\,\mathrm{J/cm^2}$ and $N_z = 25$ as laser peak fluence and number of scans, respectively.

6 Results and discussion

LMFBGs with four different groove widths were processed and analyzed. For an analysis of the groove widths, we used a standard light microscope. Figure 5 depicts light microscope images of the LMFBG structures with measured widths at the top of the grooves of $b = 47$, 85, 135 and 201 µm. The measurements shown represent the widths at a single azimuthal position.

When measured at twelve equally spaced azimuthal angles, the averaged widths yield 48, 87, 135 and 205 µm, each with a standard deviation of 3 µm (see Table 1). These LMFBGs were produced with nominal values of groove widths of $b^* = 40$, 80, 120 and 200 µm, respectively. Therefore, the measured groove widths were actually larger than the corresponding nominal values by 5–15 µm.

All LMFBGs exhibited almost parallel and steep sidewalls when inspected under the light microscope. To get further information on the spatial properties we additionally used confocal imaging microscopy. As examples, Fig. 6 depicts two height profiles that were extracted from the confocal images. In this figure, the height profiles show that the edges have certain slopes. For the 48 µm LMFBG (Fig. 6a), the sidewall angles amount to −60° for the left and 82° for the right edge. The widths on the top and the bottom of the groove have values of about 48 and 30 µm, respectively. For the 135 µm LMFBG the corresponding values for the left and right sidewall angles as well as for the top and bottom groove widths are −75°, 72°, 135µm and 108µm (see Fig. 6b).

In both cases, the sidewall angles have not the ideal values of 90° and the removed material geometries correspond to a trapezoid and deviate significantly from an ideal square. With respect to the beam caustics of a focused laser beam and under the assumption of a focus radius of $w_{\mathrm{eff}} = 1.6\,\mu\mathrm{m}$ and an ideal Gaussian beam, a far field divergence angle of about 12° can be expected. This would result in maximum sidewall angles of ± 78 °. By taking into account a non-ideal Gaussian beam and process inhomogeneity due to the non-linear character of the machining, combined with measurement uncertainties of the confocal microscope used, the observed values for the sidewall angles ranging from 60° to 82° can be understood. With the data obtained from confocal images, an analysis regarding the processed actual depth d was performed. From a series of confocal images that have been taken at different azimuthal angles, the depth of the structure could be measured and thus the roundness of the ablated cylinder and its alignment with the fiber axis could be assessed. Figure 7 displays a polar diagram of the measured radii in dependence on the azimuthal angle in 30° steps for the four LMFBGs.

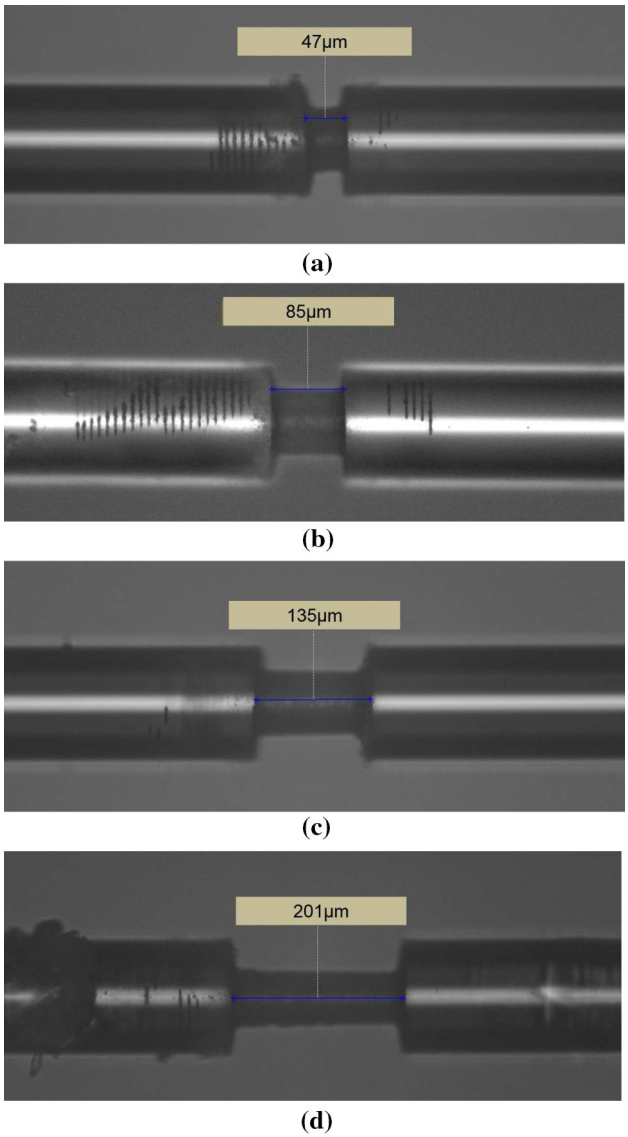

Fig. 5 Light microscope images of LMFBGs with different groove widths at 10× magnification. From image a) to d) the measured groove widths rounded to a full micrometer are $b = 47$, 85, 135 and 201 µm, as indicated by blue lines. The vertical black lines on the fiber surfaces are residuals from the focus finding routine

According to the diagram in Figure 7, all LMFBGs except for the 205 µm LMFBG exhibit a round and concentric shape with radii in the range from 31.5 to 37.5 µm. Typically, the ratio of the minimum remaining radius divided by the maximum remaining radius is 0.85 for these LMFBGs. The 205 µm LMFGB exhibits a ratio of only about 0.75, resulting in an elliptical shape. Between 240° and 330°, the remaining radii of the 205 µm LMFBG show a significant deviation from the nominal value with noticeably low values in the range from 24.5 to 28.5 µm. Positioning uncertainties, comprising a value of ± 2 µm for the z-zero position finding routine and ± 1 µm for z-translation

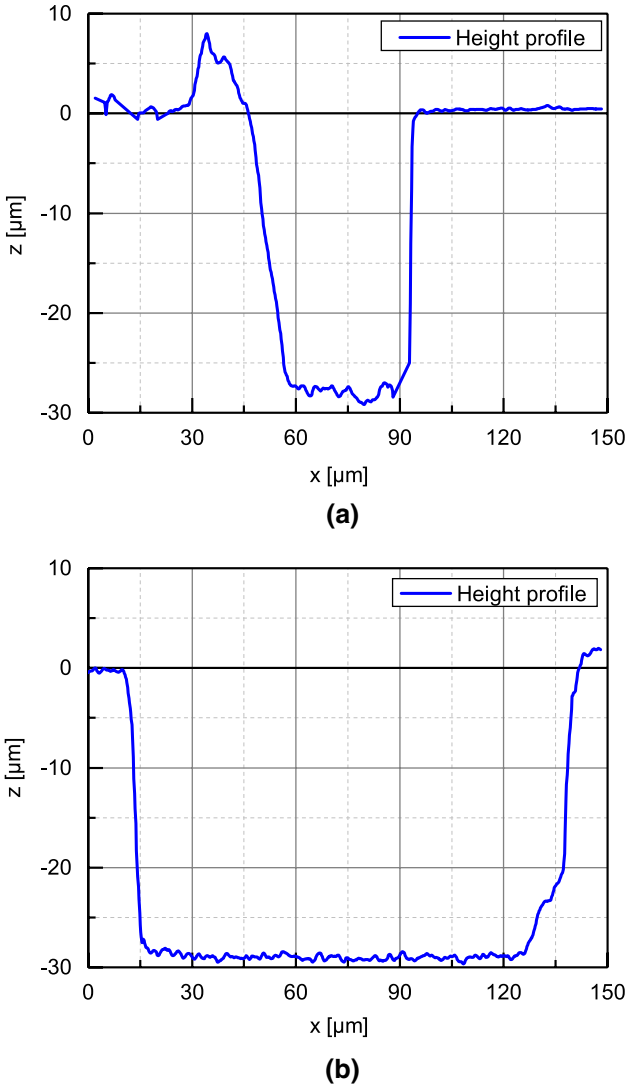

Fig. 6 Height profiles obtained by confocal microscopy of LMFBGs with groove widths $b = 48$ µm (**a**) and $b = 135$ µm (**b**). The steepness of the edges is evaluated by their sidewall angles that are estimated to −60° for the left and 82° for the right edge of the 48 µm LMFBG. For the 135 µm LMFBG, sidewall angles correspond to −75° for the left and 72° for the right edge. Consequently, different widths are measured at the top (48 µm) and the bottom (30 µm) of the groove for the 48 µm LMFBG. For the 135 µm, LMFBG groove widths yield 135μm on the top and 108 µm on the bottom

stage can contribute to the deviation of nominal and actual radii in the order of ± 3 µm. This explains well the deviations observed in the 48, 87 and 135 µm LMFBGs. Most likely, an inaccurate alignment of the stage-system has led to an elliptical rotation of the fiber and thus caused the larger deviation of the 205 µm LMFBG. The roughness at the bottom of the grooves, calculated by the standard deviation of the measured depths along the fiber axis at a single azimuthal position, exhibits values of ± 0.3–± 0.8 µm.

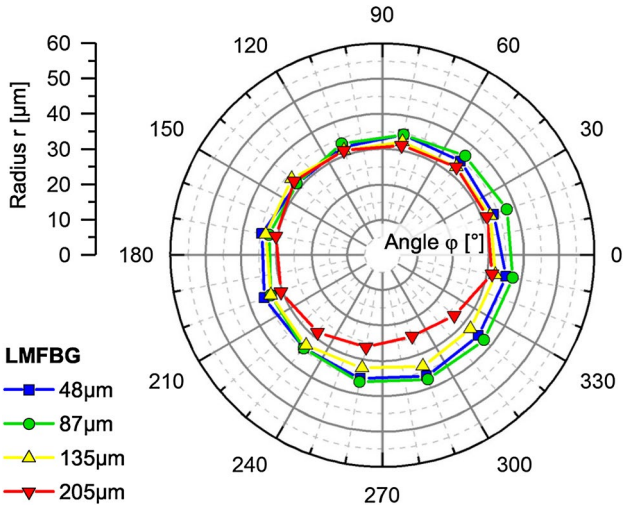

Fig. 7 Polar diagram with cross sections of all LMFBGs displaying the remaining radius r in dependence on the azimuthal angle φ

Table 1 Results of the geometrical analysis of the LMFBG images recorded in azimuthal angle steps of 30°

LMFBG	Av. Groove width b µm	Average Radius r µm	Ratio r_{min}/r_{max}	Groove roughness µm
48	48 ± 3	34.5 ± 1.4	0.86	± 0.5
87	87 ± 3	35.3 ± 2.2	0.84	± 0.3
135	135 ± 3	32.8 ± 0.7	0.94	± 0.6
205	205 ± 3	29.8 ± 2.7	0.75	± 1.0

The azimuthally averaged groove widths, b, and radii, r, as well as the ratios of the minimum and maximum radii of the LMFBGs are given. The uncertainties are the empirical standard deviations of all averaged values. The values of groove roughness correspond to the empirical standard deviations of measured groove depths at a single azimuthal position

Table 1 summarizes the geometrical analysis of the data acquired by light microscope and confocal microscope.

For a rough estimate of the laser processing energetics, the ablation efficiency E/V is considered. Here, the dose E is the total energy accumulated over all incident pulses and V is the ablated volume. The total energy dose used for the ablation equals

$$E = \overline{P} \times t \times N_x \times N_z \tag{3}$$

with the averaged laser power, $\overline{P} = 111$ mW, the duration time for one rotation, $t = 9$ s, and the number of x- and z-scans, N_x and N_z, respectively. The determined ablated volume can be calculated by subtracting the volume of the remaining fiber segment of averaged radius r from a cylinder with the groove length b (values see Table 1) and the initial fiber radius $r_F = 62.5$ µm:

$$V = (r_F^2 \times \pi - r^2 \times \pi) \times b. \quad (4)$$

Table 2 gives an overview of the deposited energy dose, the ablated volumes and the corresponding ablation efficiencies for all four samples which have been processed. In our experiments, the ablation efficiency was 1.3–1.4 MJ/mm^3. The typical total evaporation enthalpy of a solid lies in the range of 50–100 J/mm^3 [26]. For ultrashort single pulses, the energetics at laser ablation threshold corresponds to an energy per volume, which is close to the evaporation enthalpy. On ultrashort time scales the dominant ablation mechanism is mainly evaporation and not liquid dynamics or melt ejection, as it is the case for ns-pulses [30]. The dose per volume for the most efficient ultrashort pulse laser ablation of solids lies in the range of 500–1000 J/mm^3 [28, 31].

Table 2 Calculated ablation efficiencies of the machining processes for the produced LMFBGs

LMFBG (µm)	Cumulated energy dose (J)	Ablated volume (mm^3)	Ablation efficiency (J/mm^3)
48	499.4	4.0×10^{-3}	1.3×10^6
87	998.9	7.3×10^{-3}	1.4×10^6
135	1498.3	12.0×10^{-3}	1.3×10^6
205	2497.2	19.4×10^{-3}	1.3×10^6

Compared to these values, the ablation efficiencies from Table 2, which lie in the order of 1.3 MJ/mm^3, represent three orders of magnitude higher energy irradiation. This is obviously caused by the large overlap of 99.98% (PPP = 4400) which even increases when the fiber diameter decreases during the fs-laser processing (see Sect. 5). The high pulse overlap has been chosen in order to achieve a smooth and almost ideal optical surface quality and steeper edges, although it represents a trade-off with regard to ablation efficiency. Here, steep groove walls are important because they allow to model the sensor element as a combination of three distinct sections, as described in [23]. This model approach, consisting of a three-element transfer matrix, cannot be applied to LMFBGs produced by alternative techniques [10–15], because these techniques only allow gradual variations of the fiber diameter that extend over distances in the order of 1 mm. As an example, Figure 8 depicts reflection spectra of the 135 µm LMFBG at certain reference values of axial compressive forces at room temperature. Theoretical line shapes, based on the three-element transfer matrix model have been fitted to the experimental data with temperature and force as the free-fitting parameters, as described in [23]. As can be seen in Fig. 8, the measured

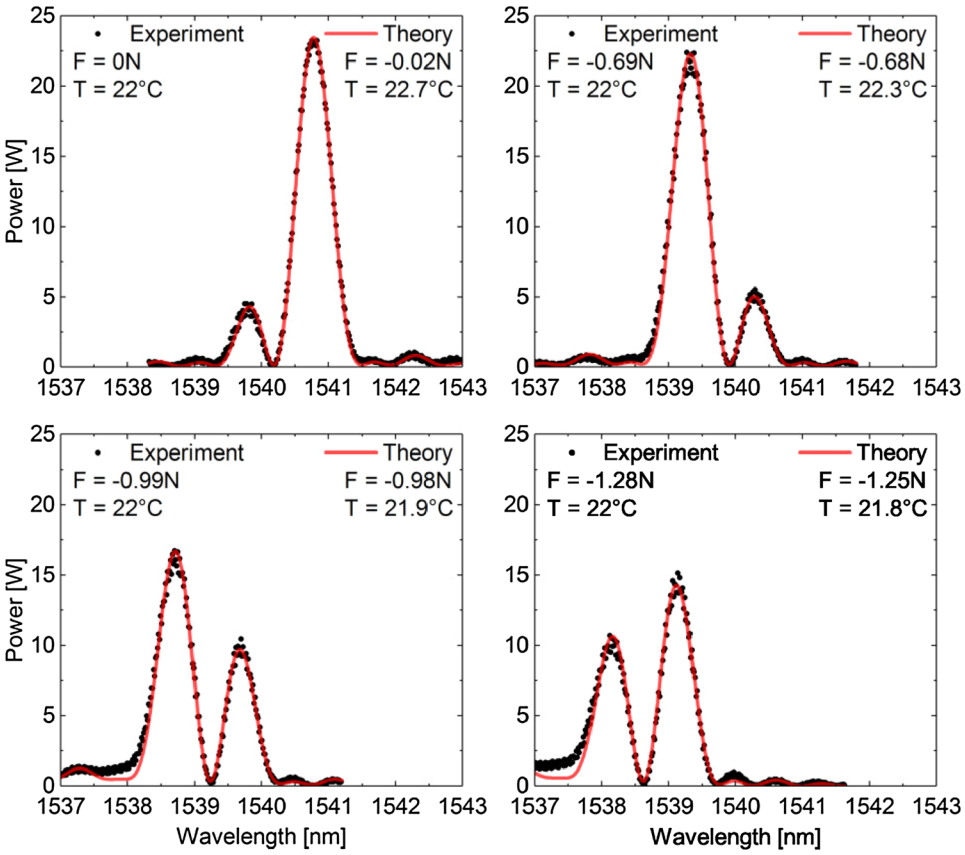

Fig. 8 Reflection spectra of the 135 µm LMFBG at compressive reference forces from 0 to 1.28 N and reference temperature (data in the upper left). The force and temperature values derived from fitting theoretical line shapes to the measured spectra (data in the upper right) agree well with the corresponding reference values

lines data are in good accordance with the theoretical line shapes and thus the force and temperature values obtained by the fits to the spectra agree well with the corresponding reference values.

7 Conclusion

In this article, we describe the fabrication of four LMFBGs with different groove widths by fs-laser processing in a specially designed machining system. Observed with a light microscope, the structured grooves indicate selective and homogenous profiles with steep edges. Furthermore, confocal images have provided quantitative information on the geometry of the LMFBGs. The slopes of the edges show angles of 60°–82° with respect to the surface. The widths at the surface of the grooves are 5–15 µm larger than the corresponding desired widths. The resulting depths of the structures, indicated by the azimuthally averaged radii, deviate less than 3 µm from the targeted value of 32.5 µm. However, the LMFBG with the largest groove width exhibits outliers of the remaining radii over a certain angle range, resulting in an elliptical shape. To obtain a precise morphology with smooth micro-structured surfaces, a high pulse overlap (respectively number of pulses per position) was employed, resulting in a process not optimized with regard to ablation efficiency. Exemplarily shown reflection spectra of one of the LMFBG sensors produced by the machining process are in good agreement with theoretical model calculations. Here, the goal was to create grooves with steep sidewalls to keep the theoretical model, which considers only three distinct fiber sections, as simple as possible. The LMFBGs may find applications as sensors for simultaneous force and temperature measurements with enhanced force sensitivities. Future tasks will be the improvement of the ablation efficiency and the fabrication accuracy, and the reduction of processing time. Due to the high flexibility of the fabrication technique, we will investigate different micro-structured geometries with further improved sensing characteristics in the future.

Funding This work was partly supported by the "Bayerische Forschungsstiftung", reference no. AZ-1146-14.

References

1. H. Xia, Proc. SPIE **8370**, 83700F (2012)
2. M. Willsch, T. Bosselmann, M. Villnow, W. Ecke, Proc. SPIE **8421**, 84210R (2012)
3. D. Kinet, P. Mgret, K.W. Goosen, L. Qiu, D. Heider, C. Caucheteur, Sensors **14**(4), 7394 (2014)
4. R. Di Sante, Sensors **15**(8), 18666 (2015)
5. P. Roriz, L. Carvalho, O. Frazo, J.L. Santos, J.A. Simes, J. Biomech. **47**(6), 1251 (2014)
6. A.A.G. Abushagur, N. Arsad, M.I. Reaz, A. Ashrif, A. Bakar, Sensors **14**(4), 6633 (2014)
7. G. Marchi, V. Baier, P. Alberton, P. Foehr, R. Burgkart, A. Aszodi, H. Clausen-Schaumann, J. Roths, Sens. Actuators B **252**, 440 (2017)
8. A. Kersey, M. Davis, H. Patrick, M. LeBlanc, K. Koo, C. Askins, M. Putnam, E. Friebele, J. Lightwave Tech. **15**(8), 1442 (1997)
9. O. Frazo, L. Ferreira, F. Arajo, J. Santos, Fiber Integr. Opt. **24**(3–4), 227 (2005)
10. A. Cusano, D. Paladino, A. Iadicicco, J. Lightwave Technol. **27**(11), 1663 (2009)
11. A. Iadicicco, S. Campopiano, A. Cutolo, M. Giordano, A. Cusano, Electron. Lett. **41**(8), 466 (2005)
12. A. Cusano, A. Iadicicco, D. Paladino, S. Campopiano, A. Cutolo, Opt. Express **16**(20), 15332 (2008)
13. A. Iadicicco, S. Campopiano, D. Paladino, A. Cutolo, A. Cusano, Opt. Express **15**(23), 15011 (2007)
14. A. Iadicicco, S. Campopiano, A. Cutolo, M. Giordano, A. Cusano, IEEE Photonics Technol. Lett. **17**(6), 1250 (2005)
15. A. Cusano, A. Iadicicco, D. Paladino, S. Campopiano, A. Cutolo, M. Giordano, Opt. Fiber Technol. **13**(4), 281 (2007)
16. R.R. Gattas, E. Mazur, Nat. Photonics **2**, 219 (2008)
17. A. Martinez, M. Dubov, I. Khrushchev, I. Bennion, Electron. Lett. **40**(19), 1170 (2004)
18. S.J. Mihailov, C.W. Smelser, D. Grobnic, R.B. Walker, P. Lu, H. Ding, J. Unruh, J. Lightwave Technol. **22**(1), 94 (2004)
19. Z.L. Ran, Y.J. Rao, W.J. Liu, X. Liao, K.S. Chiang, Opt. Express **16**(3), 2252 (2008)
20. Y.J. Rao, M. Deng, D.W. Duan, X.C. Yang, T. Zhu, G.H. Cheng, Opt. Express **15**, 14123 (2007)
21. F. Albri, J. Li, R.R. Maier, W.N. MacPherson, D.P. Hand, J. Micromech. Microeng. **23**(4), 045021 (2013)
22. Y. Dai, M. Yang, G. Xu, Y. Yuan, Opt. Express **21**(14), 17386 (2013)
23. G. Marchi, V. Stephan, F.J. Dutz, B. Hopf, L. Polz, H.P. Huber, J. Roths, J. Lightwave Tech. **34**(19), 4557 (2016)
24. F.J. Dutz, G. Marchi, V. Stephan, H.P. Huber, J. Roths, Proc. SPIE **9916**, 1 (2016)
25. G. Marchi, V. Stephan, F.J. Dutz, H.P. Huber, J. Roths, Proc. SPIE **9886**, 1 (2016)
26. G. Heise, M. Englmaier, C. Hellwig, T. Kuznicki, S. Sarrach, H.P. Huber, Appl. Phys. A **102**, 173 (2011)
27. B.C. Stuart, M.D. Feit, S. Herman, A.M. Rubenchik, B.W. Shore, M.D. Perry, Phys. Rev. B **53**(4), 1749 (1996)
28. N. Varkentina, N. Sanner, M. Lebugle, M. Sentis, O. Utza, J. Appl. Phys. **114**(173105), 1731051 (2013)
29. I. Mirza, N.M. Bulgakova, J. Tomstk, V. Michlek, O. Haderka, L. Fekete, T. Mocek, Sci. Rep. **6**(39133), 1 (2016)
30. M. Domke, L. Nobile, S. Rapp, S. Eiselen, J. Sotrop, H.P. Huber, M. Schmidt, Phys. Proc. **56**, 1007 (2014)
31. B. Neuenschander, B. Jaeggi, M. Schmid, V. Rouffiange, P.E. Martin, Proc. SPIE **8243**, 824307 (2012)